

# Toughness by segmentation: Fabrication, testing and micromechanics of architected ceramic panels for impact applications

Mohammad Mirkhalaf<sup>a,b</sup>, Amanul Sunesara<sup>b</sup>, Behnam Ashrafi<sup>b,\*</sup>, Francois Barthelat<sup>a,\*</sup>

<sup>a</sup> Department of Mechanical Engineering, McGill University, 817 Sherbrooke Street West, Montreal, Quebec H3A 2K6, Canada

<sup>b</sup> Structures, Materials and Manufacturing Laboratory, National Research Council of Canada, 5145 Decelles Avenue, Montreal, Quebec H3T 2B2, Canada

## ARTICLE INFO

### Article history:

Received 13 February 2018

Revised 12 August 2018

Available online 28 August 2018

### Keywords:

Bio-inspiration

Architected materials

Topologically interlocked materials

Ceramics

Impact loading

Out-of-plane loading

## ABSTRACT

Precise material architectures and interfaces can generate unusual and attractive combinations of mechanisms and properties. For example, the segmentation into blocks of finite size and well-defined geometries can turn brittle ceramics into tough, deformable and impact resistant material systems. This strategy, while scarcely used in engineering, has been successfully used for millions of years in biological materials such as bone, nacre or tooth enamel. In this work, the precise relationships between architecture, mechanics, and properties in architected ceramic panels are explored using a combination of mechanical testing with stereo-imaging, 3D reconstruction, and finite-element/analytical modeling. In particular, this work shows that a fine balance of interlocking and block size generates controlled frictional sliding and rotation of blocks, minimizes damage to individual blocks and optimizes performance. These ceramic architected panels have 1/4 to 1/2 of the strength of monolithic ceramic panels, but they can absorb 5 to 20 times more mechanical energy, making them very attractive for applications where high surface hardness or high resistance to temperature must be combined with resistance to impact and toughness.

© 2018 Elsevier Ltd. All rights reserved.

## 1. Introduction

Ceramics are attractive engineering materials because of their high stiffness and strength, low density, excellent thermal stability, and high oxidation/corrosion resistance. However, the main weakness of ceramics is their brittleness, which remains a major limitation despite significant research efforts (Evans, 1990). Interestingly, biological materials can achieve surprisingly high combinations of toughness and strength (Ritchie, 2011) and overcome the brittleness of biominerals in bone (Koester et al., 2008), nacre (Barthelat and Rabiei, 2011), tooth enamel (Yahyazadehfar et al., 2014), or sponge spicules (Aizenberg et al., 2005) (Fig. 1). While these materials all display a complex hierarchical microstructure, meso-scale elements appear to be the most important for toughness: osteons in bone, tablets in nacre, rods in enamel, and layers in sponge spicules. As a universal construction rule, these materials are made of hard and stiff mineral building blocks bonded by weaker interfaces (Barthelat, 2015; Barthelat et al., 2016). These finely tuned architectures can result in useful deformation/failure mechanisms which give rise to amplifications of toughness so far unmatched in engineering materials. For example, the staggered

architecture of nacre results in mechanisms such as progressive tablet sliding, crack blunting/deflecting/bridging, and process zone, mechanisms which make nacre three orders of magnitude tougher than its main constituent, aragonite (Barthelat and Rabiei, 2011; Jackson et al., 1988; Slesarenko et al., 2017b; Wang et al., 2001). These principles are now inspiring new classes of architected materials with interesting combination of properties and functionalities (Dyskin et al., 2001; Lin et al., 2014; Mirkhalaf and Ashrafi, 2017; Mirkhalaf and Barthelat, 2015; Mirkhalaf and Barthelat, 2016; Mirkhalaf et al., 2018; Rudykh et al., 2015).

Geometrical interlocking can be used in architected materials as a strain hardening mechanism to delay localization and spread the deformation to a large volume of material (Fig. 1d) (Barthelat, 2015). The resulting materials are called “topologically interlocked materials” (TIMs) (Djumas et al., 2017; Dyskin et al., 2003a; Siegmund et al., 2016). The geometrical features of these materials are the intermediate length scales between microstructural length scales (grain size in metals) and size of the component (Fig. 1e) (Barthelat, 2015; Brechet and Embury, 2013). Because of this intermediate length scale, full control over the morphology can be achieved using precise manufacturing techniques. Bottom-up as well as top-down procedures have been used for the fabrication of TIMs (Siegmund et al., 2016). In the bottom-up approach, building blocks are first fabricated and then assembled. The blocks have been made through techniques such

\* Corresponding authors.

E-mail addresses: [behnam.ashrafi@nrc-nrc.gc.ca](mailto:behnam.ashrafi@nrc-nrc.gc.ca) (B. Ashrafi), [francois.barthelat@mcgill.ca](mailto:francois.barthelat@mcgill.ca) (F. Barthelat).

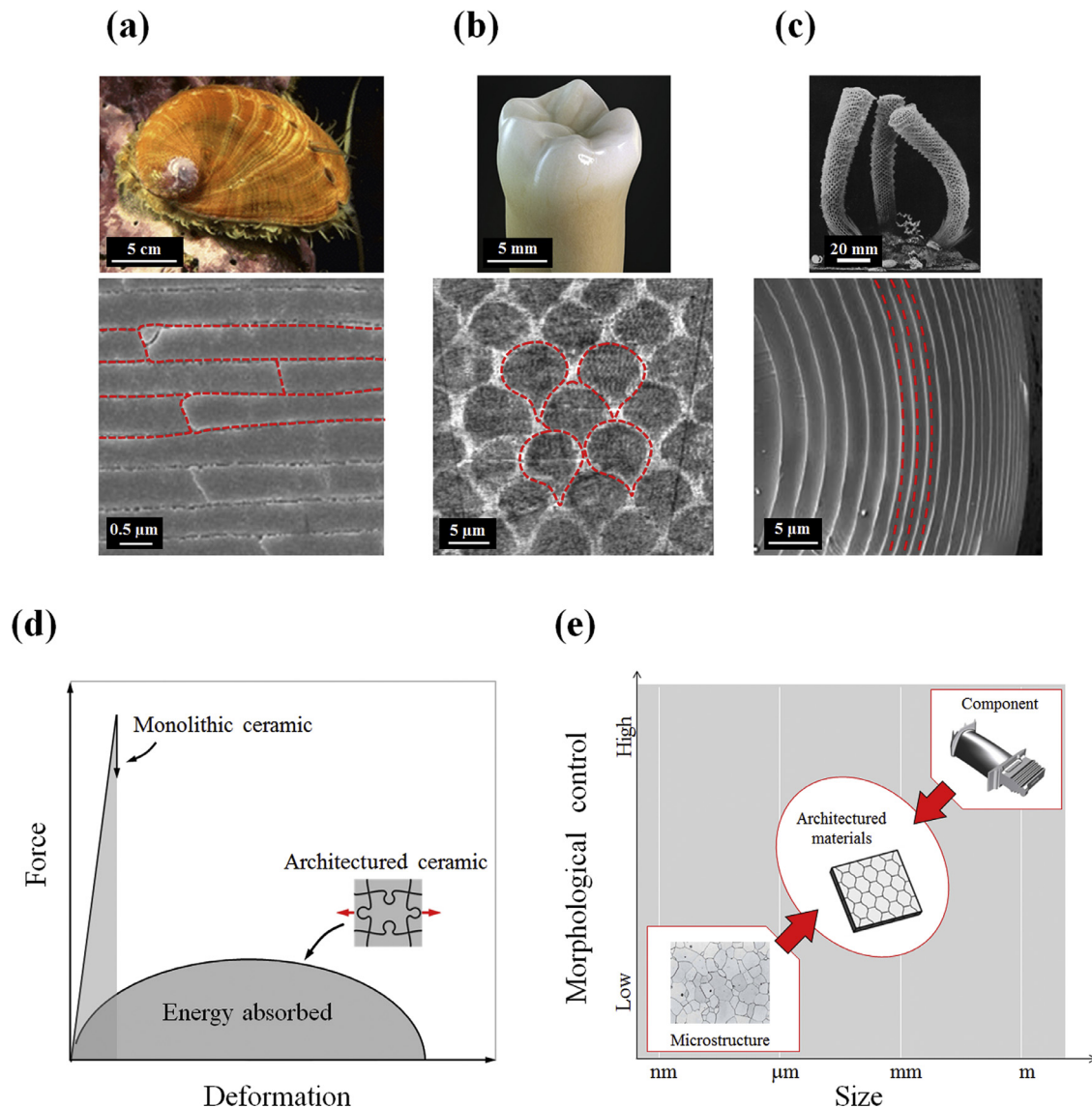


**Fig. 1.** Architecture, weak interfaces and interlocking principles in biological materials inspire new classes of engineering materials. (a) The inner layer of sea shell is composed of aragonite tablets which are arranged in a staggered structure (adapted from (Barthelat and Zhu, 2011)). (b) Tooth enamel is composed of mineral rods which are aligned perpendicular to its surface and are separated by soft bio-polymeric interfaces (adapted from Habelitz et al., 2001). (c) Spicules of glass sponge skeleton is composed of concentric glass cylinders (adapted from Aizenberg et al., 2005). The borders of building blocks are shown with dashed red line in panels a–c. (d) The concept of architected materials: materials with designed morphologies at length scales where full control over the morphology is achievable. (e) Deformation behavior of architected versus monolithic ceramics. (For interpretation of the references to color in this figure legend, the reader is referred to the web version of this article.)

as 3D printing (Djumas et al., 2017; Feng et al., 2015; Khandelwal et al., 2015; Malik et al., 2017; Slesarenko et al., 2017a), and casting (Krause et al., 2012; Mirkhalaf et al., 2018) and of variety of shapes such as regular tetrahedral (Khandelwal et al., 2012, 2014), osteomorphic (Autruffe et al., 2007; Dyskin et al., 2003b; Javan et al., 2017), regular cubes (Dugue et al., 2013; Estrin et al., 2004), buckyballs (Dyskin et al., 2003a), jigsaw (Mirkhalaf et al., 2014), or puzzle-like shapes (Haldar et al., 2017; Mirkhalaf and Barthelat, 2017). These blocks are then assembled through precise methods: manual assembly (Krause et al., 2012), robotic pick and place (Mather et al., 2012), template assisted parallel assembly (Mather, 2007), self-assembly (Mirkhalaf et al., 2015; Siegmund et al., 2016), or by embedded wires (Siegmund et al., 2013). In the top-down approach, the interfaces are carved within the bulk of material, in effect producing a well-controlled architecture. We recently demonstrated that top-down laser engraving can be used to develop three-dimensional architectures within glass which result in improved resistance to in-plane (Mirkhalaf and Barthelat, 2015;

Mirkhalaf et al., 2014) or out-of-plane loads (Mirkhalaf et al., 2016) and in different loading conditions: quasi-static (Mirkhalaf and Barthelat, 2015) as well as impact (Mirkhalaf et al., 2016). TIMs can possess other interesting properties such as quasi-ductile behavior (Dyskin et al., 2003a,b; Khandelwal et al., 2012; Schaare et al., 2008), localized damage (Dyskin et al., 2003b), and the ability to be reconstructed (Mather et al., 2012).

Different materials such as polymers, metals/alloys, ceramics/glasses, and ice have been used for construction of TIMs (Siegmund et al., 2016). Application of TIMs for ceramics and glasses is particularly promising because topological interlocking and weak interfaces introduce toughening mechanisms such as crack blunting and frictional sliding into these materials, mechanisms which can address the inherent brittleness of these materials. In this study, we develop a simple and versatile cutting/assembly technique to fabricate topologically interlocked ceramic panels. Novel structure-property relations in these panels are revealed using experiments under stereo-imaging, 3D reconstruct-

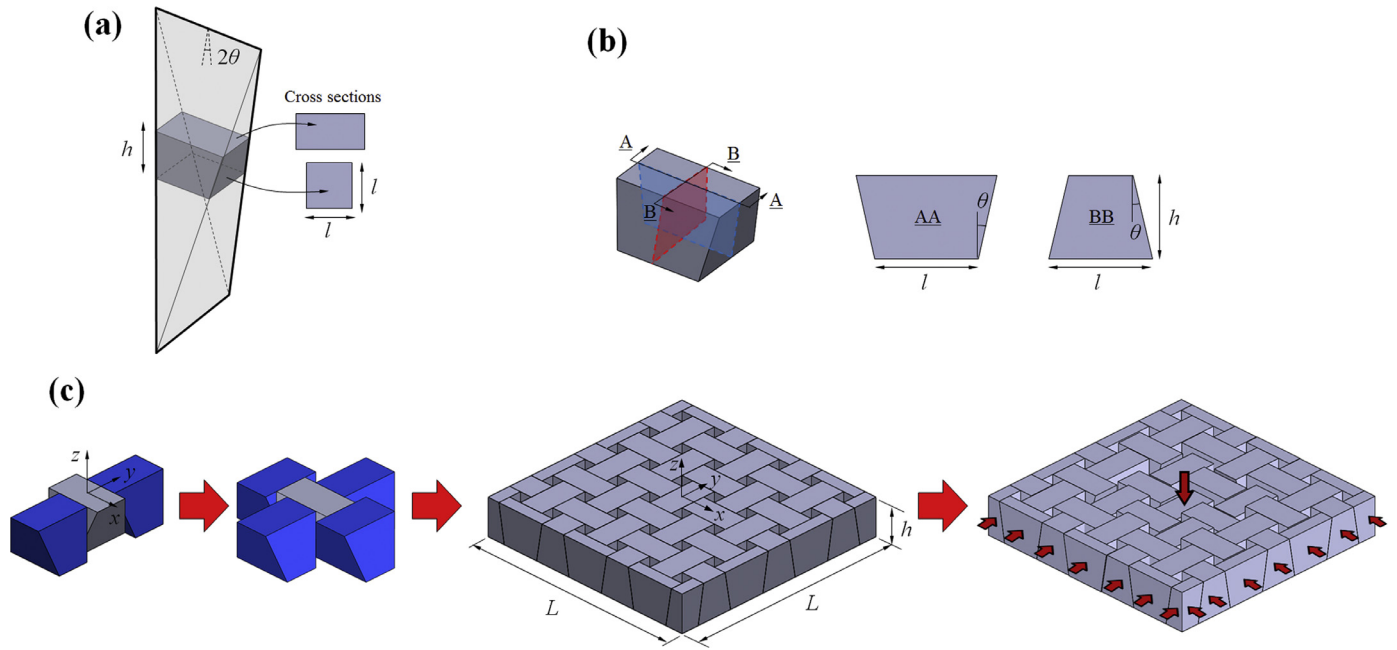


**Fig. 2.** Overview of the design of interlocked panels. (a) Individual building blocks are obtained from truncating a tetrahedron. (b) Geometry of the building blocks, showing the locking angle  $\theta$ . (c) how a block is constrained or “topologically interlocked” by its neighbors, e. g. in a  $5 \times 5$  architected panel developed in this study, and how the blocks move under loading. The truncated blocks at the edges are used to impose in-plane confinement required for interlocking.

tion, finite element analysis (FEA) and analytical modeling. The resulting ceramic panels are found to be 5 to 20 times more impact resistant than their monolithic counterparts.

## 2. Design and fabrication of architected ceramic panels

The architected ceramic panels we explored in this study were assembled from truncated tetrahedral blocks (Fig. 2). In contrast to the fixed geometry of platonic tetrahedral blocks used previously in topologically interlocked panels (Dyskin et al., 2003a; Feng et al., 2015), our truncated version is based on a non-platonic tetrahedron with more freedom to finely tune the geometry and therefore optimize the mechanical performance (Mirkhalaf et al., 2016). Moreover, the truncated version has a larger contact area. For example, a truncated tetrahedron with  $\theta = 5^\circ$  (Fig. 2b) has a contact area with its neighbors which is 54% greater than when regular tetrahedra of the same height are used. The truncated version also has planar top and bottom surfaces, which facilitate assembly and enhances the mechanical durability of the surfaces. The geometry of the blocks obtained by truncating a non-regular tetrahedron at the median plane (a square, Fig. 2a) and at a plane at a distance  $h$  from that median plane. The resulting block has six faces, with the two facing surfaces tilted inward and the other two surfaces tilted outward by the same “interlocking angle”  $\theta$  (Brocato and Mondardini, 2012) (Fig. 2b). The top and bottom surfaces are parallel. The lower face of the building block is an  $l \times l$  square, while the top face is a rectangle of dimensions  $l + 2htan\theta$  by  $l - 2htan\theta$ . The geometry of the building blocks is therefore fully characterized by the three independent parameters  $h$ ,  $l$ , and  $\theta$ . In an assembly of these blocks, the three-dimensional displacement and rotation of each of the blocks is constrained by its four neighbors (Fig. 2c). This basic assembly procedure can be repeated in the  $x$ - $y$  plane to make large arrays of blocks which are interlocked and can keep their position without the need for any adhesive or other fastening, provided that the edge of the panel is constrained by a rigid frame which serves as “external ligament” for the assembly (Fig. 2c).

When the panel is subjected to a quasi-static transverse force (or an impact), the relative sliding and rotation of the blocks generates overall large deformations, while individual blocks do not deform significantly (Fig. 2c). Since these relative motions entail frictional sliding, the panel should also absorb much more mechanical energy than a monolithic panel made of the same material. The objective is to use these deformation mechanisms to produce the force-displacement response shown in Fig. 1e, where the architecture and controlled deformations at the interfaces of the blocks generate new mechanisms, large deformations and energy absorption in an otherwise all brittle material.

To produce our panels, individual blocks were cut from a high-density (porosity < 2% vol., McMaster Carr, IL, US) unfired alumina silicate plate with thickness  $h = 3.18$  mm. The plate was fixed onto a wedged platform with adjustable angle  $\theta$ , and were then cut using a precision diamond saw (Struers, OH, US, Fig. 3a), which yielded uniform blocks with smooth surfaces, which were then assembled manually. Individual blocks were fed manually on a smooth inclined plate, using a right-angled corner as a template (Fig. 3b). The blocks slid into place against the template and then against each other, so that there were no gaps between the blocks in the final assembly. The peripheral blocks were cut so that the sides of the panel presented vertical surfaces, a requirement for a proper constraint. The panels were then tape-transferred to an aluminum frame equipped with power screws which were adjusted to confine the panels with no pre-compression applied. Once the blocks were in place in that frame, the tape was removed. In this study we changed the architecture of the panels, but we maintained their overall dimensions: sides  $L \times L = 50 \times 50$  mm<sup>2</sup>, thickness  $h = 3.18$  mm (corresponding to the thickness of individual blocks). We explored the effect of interlocking angle with  $\theta = 0^\circ$ ,  $2.5^\circ$ ,  $5^\circ$ ,  $7.5^\circ$ ,  $10^\circ$ , and number of blocks with  $N \times N = 3 \times 3$ ,  $5 \times 5$  and  $7 \times 7$  (Fig. 3c). Since the size of the panel was kept constant, the corresponding lateral size of the blocks were  $l = 12.50$  mm,  $8.33$  mm and  $6.25$  mm for  $3 \times 3$ ,  $5 \times 5$  and  $7 \times 7$  arrays of blocks respectively. In addition to the architected panels, monolithic ceramics plates with identical lateral dimensions and thickness were fabricated and tested for comparison.

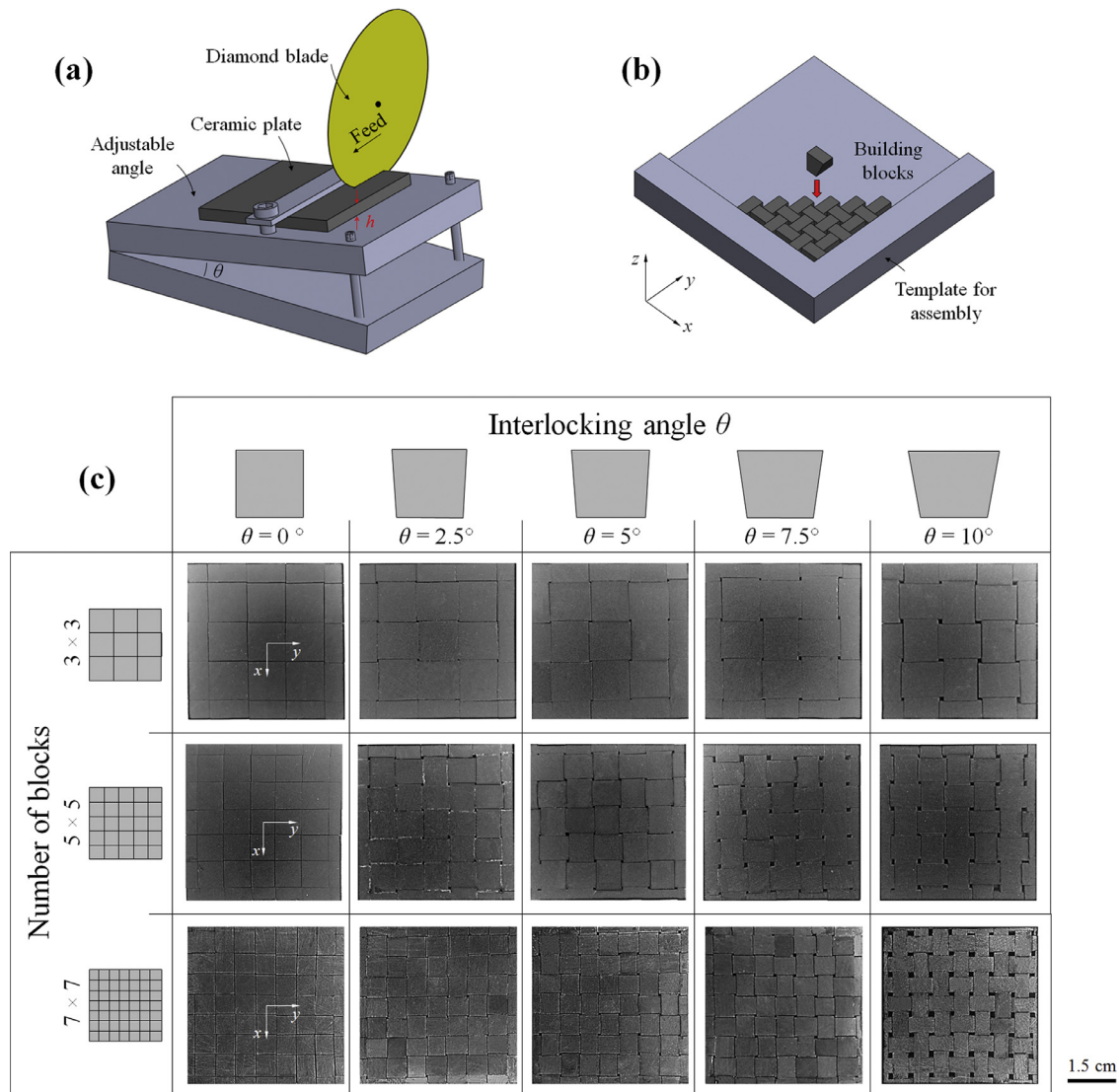


**Fig. 3.** Fabrication of architected ceramic panels. (a) The cutting set up for the fabrication of architected ceramics. (b) Schematic of the assembly set-up. (c) Architected ceramic panels with different interlocking angles ( $\theta = 0^\circ, 2.5^\circ, 5^\circ, 7.5^\circ, 10^\circ$ ) and number of blocks ( $3 \times 3, 5 \times 5$  and  $7 \times 7$  arrays of blocks).

### 3. Quasi-static response

We first examined the mechanical response of the panels when loaded by a transverse point force in quasi-static conditions. The panels were kept within a frame (Fig. 4a), but no in-plane compression was applied on the panel at the beginning of the tests. A pin with a spherical tip (tip radius = 5 mm) was used to transversely load the panels in the middle of the center block (i.e. at coordinates  $(x, y, z) = (0, 0, 0)$  on Fig. 4a). The pin was driven along  $-z$  direction at a rate of  $10 \mu\text{m/s}$  while force and displacement were recorded (Admet Dual column loading stage, MN, USA). A pair of cameras (Fastec IL5, CA, USA) was used to capture stereo-images of the surface of the panel during loading. The top surface of the panels was speckled using sprays of black and white paints for stereo image correlation. The panels were illuminated by two halogen lamps placed at two different angles to minimize the shadows of the indenter on the panel.

A representative force-deflection behavior is shown in Fig. 4b for a  $7 \times 7$ -block panel with  $\theta = 5^\circ$ , with the response from the monolithic plate for comparison. The monolithic ceramic plate showed a linear elastic response until brittle and catastrophic failure at a force  $\sim 200$  N (deflection  $\sim 0.2$  mm). Failure was dominated

by flexural cracks that emanated from the loading point and propagated rapidly to the edges of the panel (Fig. 4c). There was no indication of conical cracks at the puncture site, which indicated that the fracture of the panel was governed by flexural stresses. In contrast, the architected panels showed a bell-shaped response associated with a progressive, “graceful” type of failure. The architected panels failed by a progressive “push-out” of the center block by the loading pin, while the rest of the panel remained largely intact (Fig. 4c). The architected panel failed at a deflection of  $\sim 4$  mm (20 times the maximum deflection of the monolithic plate). We did not observe any flexural cracks in the architected panels. Segmenting the panels into building blocks decreases the span over which the flexural stresses are developed, and therefore increase the force required to induce flexural cracks (Chintapalli et al., 2014).

We used stereo-imaging and three-dimensional digital image correlation (VIC 3D, Correlated Solutions, SC, US) to determine the vertical displacement field (along the  $z$  axis, Fig. 4d) and the displacements and rotations of individual blocks (Fig. 4e–h). Using an algorithm that determined the intersection of the tetrahedral blocks, we also constructed 3D contact maps (Fig. 4g) where the red regions represent the volume of intersection (intersect vol-

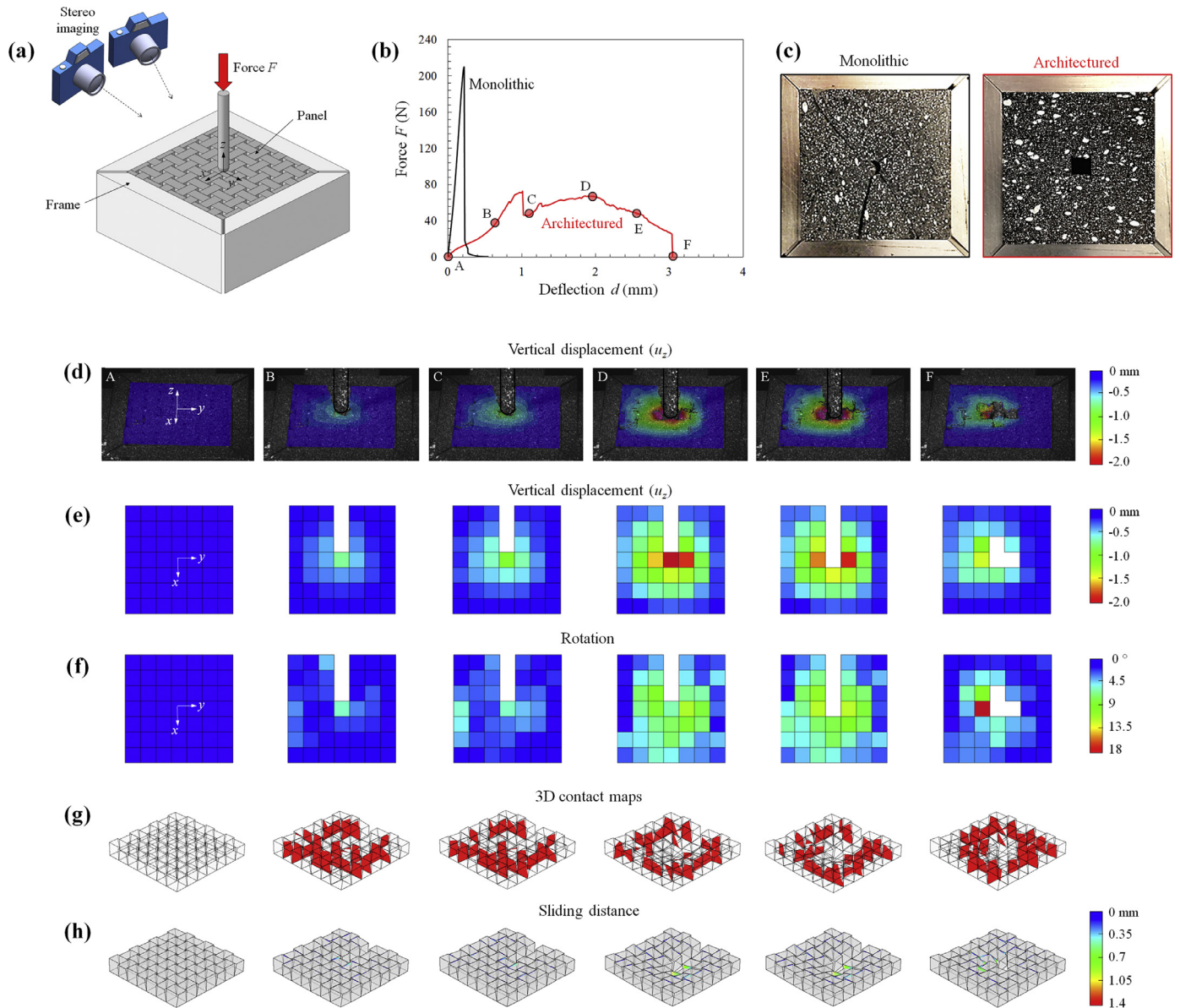


**Fig. 4.** Overview of testing of the panels in quasi-static loading. (a) Schematic of the set-up for the quasi-static tests. (b) Comparison between the force-deflection curves of the monolithic and the architected ( $7 \times 7$  sample with  $\theta = 2.5^\circ$ ) ceramic panels. (c) Images of post-mortem monolithic and architected ceramics ( $7 \times 7$  sample with  $\theta = 5^\circ$ ). (d) 3D reconstructed top surface of the architected ceramic at various stages of loading showing the displacement map of the blocks in  $z$  direction. (e) Three-dimensional digital image correlation results for the vertical displacement field at various stages of loading. (f) Rotation of the blocks at various stages of loading. (g) The contact maps between the blocks. (h) The sliding distance between the blocks. (For interpretation of the references to color in this figure legend, the reader is referred to the web version of this article.)

ume) between neighboring blocks. 3D contact maps revealed how the load was transferred between blocks, and since the deformation of individual blocks was minimal, the intersect volumes are very thin and look like surfaces. 3D reconstruction data was also used to compute the displacement jump at the interfaces between contacting blocks (revealed from the contact maps, Fig. 4g), which can be interpreted as the sliding distance between blocks (Fig. 4f). This in-depth analysis of the experiments revealed new insights on deformation and failure mechanisms, patterns of contact between blocks and total sliding distances for different designs.

Fig. 5a shows the range of mechanical responses measured from panels with fifteen combinations of interlocking angle and number of blocks. For each combination, one sample is prepared and tested. While these force-deflection curves all had a bell shape curve, the maximum displacement, forces and finer features of the curves varied significantly. These differences translated into varia-

tions in stiffness, maximum force and energy absorption (areas under the curves up to complete failure). Fig. 5b–d show how these three properties vary with design parameters. The stiffness of the panels increases with interlocking angle because of increased mechanical interaction between the blocks. The strength and energy absorption increase up to an optimum interlocking angle of  $\theta = 5^\circ$ , after which they decrease because of brittle damages to the material. This localized surface damage translated into sharp drops in the force-deflection curves, which decreased interlocking and prevented further improvement of strength and energy absorption. Finally, the results show that all properties are higher with smaller number of blocks (i.e. larger block).

These properties and performance of the architected panels can be explained and optimized by considering how individual blocks interact, slide and rotate on one another. Fig. 6a shows the force-deflection curves for designs with  $5^\circ$  interlocking angle, to-

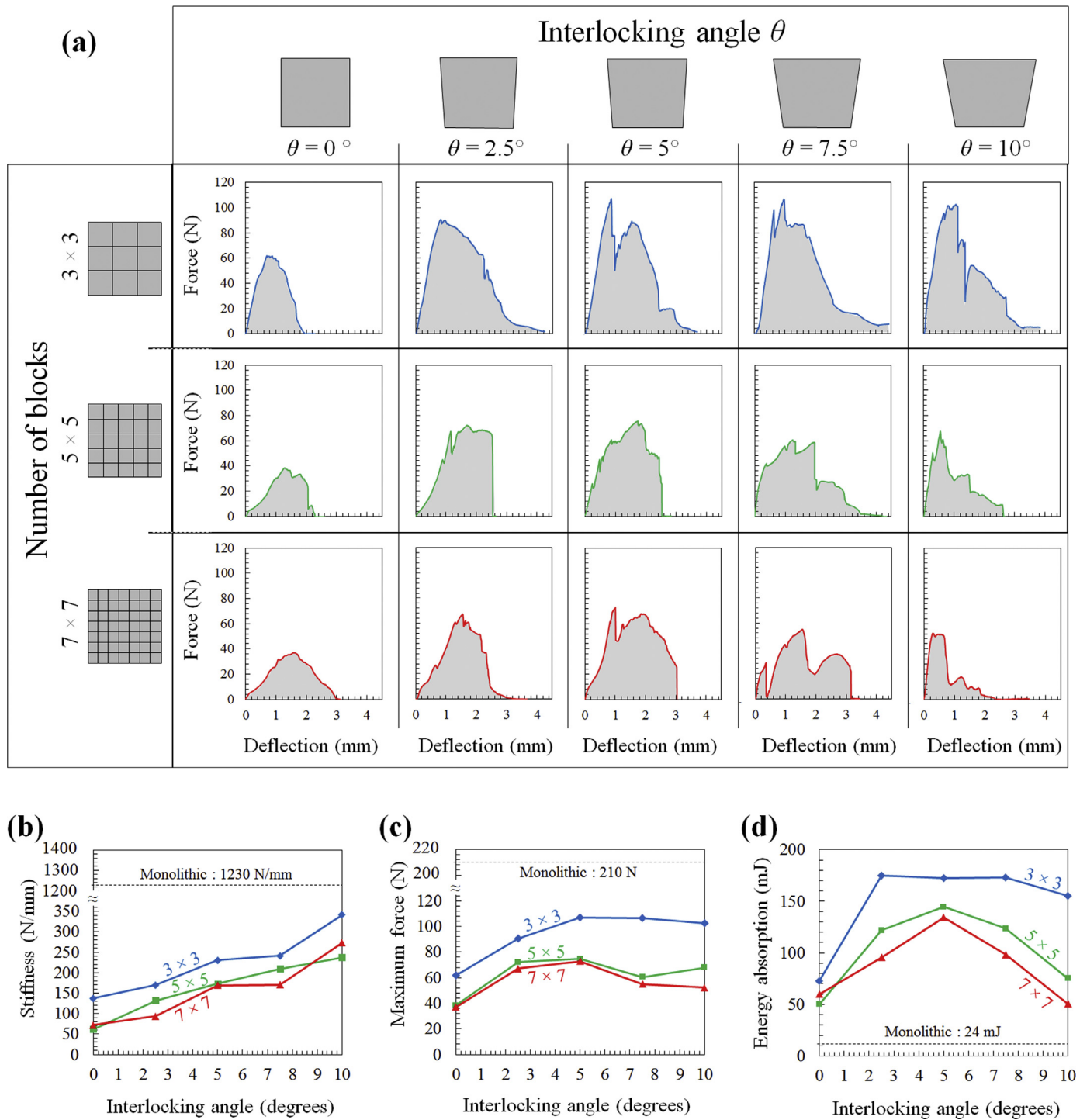


**Fig. 5.** The behavior of the architected ceramics in quasi-static loading. (a) The force-deflection response for panels with different number of blocks ( $3 \times 3$ ,  $5 \times 5$ , and  $7 \times 7$ ) and with different interlocking angles ( $\theta = 0^\circ$ ,  $2.5^\circ$ ,  $5^\circ$ ,  $7.5^\circ$ ,  $10^\circ$ ). (b) Stiffness, (c) maximum force, and (d) energy absorption of the panels as functions of interlocking angle and number of blocks.

gether with the total sliding area and the average rotation of the blocks. The total sliding area is the area over which all the blocks have slid on one another, which we measured using the sliding distance map (Fig. 4h). The average rotation is computed from the rotation of individual blocks, also measured from the stereo-imaging data. Taken together, this data reveals two distinct stages of deformation for the panels. In stage I, the force increases with deflection. Sudden drops may occur from surface damage between the blocks, but the force continues to increase throughout this stage.

In this stage, the total sliding distance and the average rotation of the blocks both increase linearly with deflection (this deformation mode is shown on Fig. 6b). The sliding and rotation of the blocks results in a progressive decrease of contact areas between the blocks, but this effect is compensated for by an increasing amount of interlocking between the blocks so that the force increases with displacement.

The deformation mode transitions from stage I to stage II when the loss of contact area prevails. In stage II sliding only occurs at

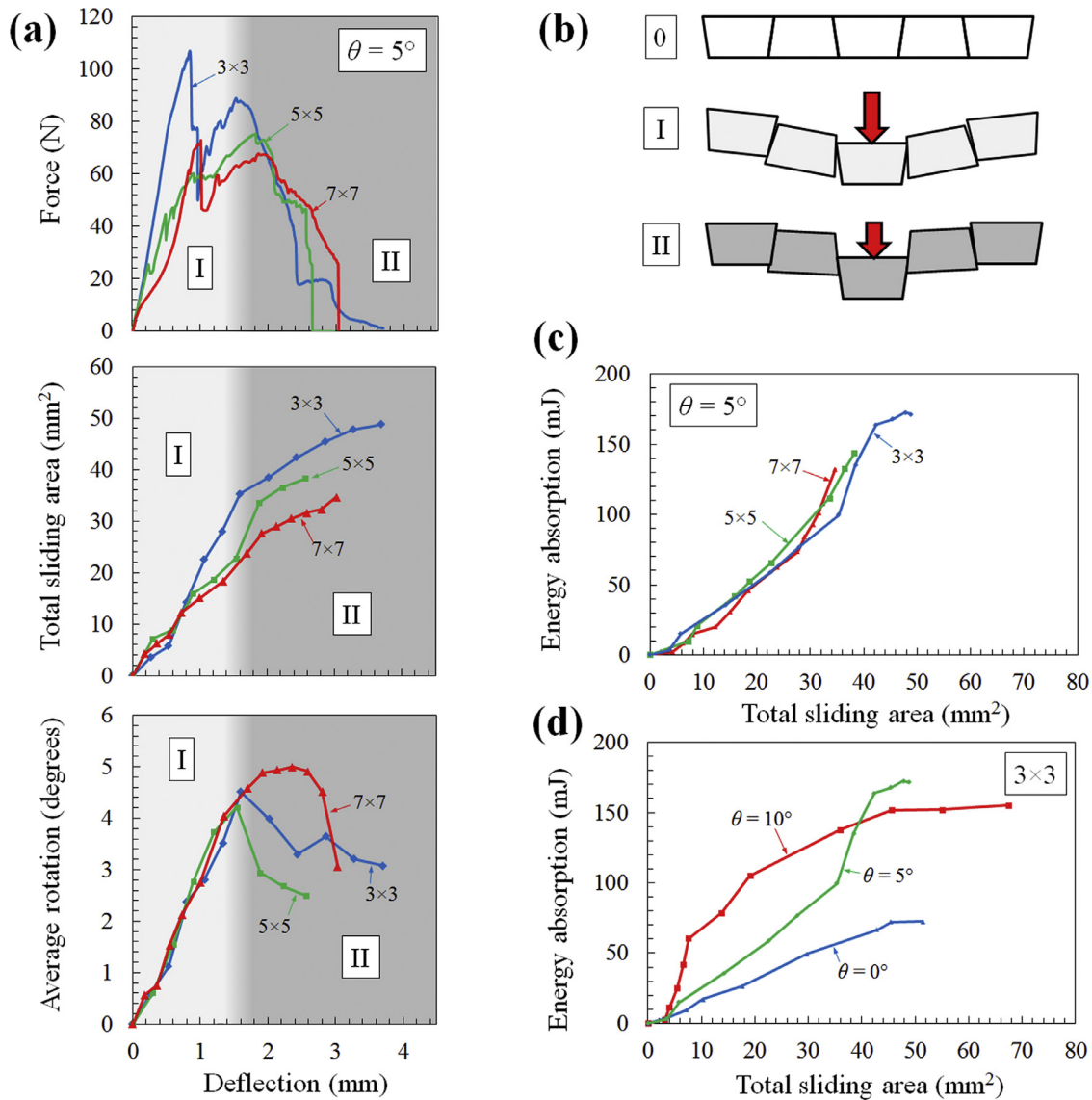


**Fig. 6.** The structure-property relations in architected panels. (a) The comparison between the force-deflection curves, total sliding area and average rotation for the panels with the same  $\theta$  and different  $N$ . (b) Schematic of the deformation of the panel during loading. (c, d) The correlation between the total sliding area and energy absorption for different  $N$  and  $\theta$ .

the interfaces of the center block. This sliding is still significant, but increases at a slower pace compared to stage I. While the center block is being pushed out and the deformation localizes, the force decreases, and the rest of the panel partially recovers its deformation. The values of residual displacement of the blocks for all the panels studied here were usually less than 1 mm (less than 1/3 of the thickness) which shows that the panels partially retained their shape after being punctured. The average rotation of the blocks reached a maximum of 4–5°, and then decreased in stage II (Fig. 6a,b).

Fig. 6c shows that the energy progressively absorbed by the panel increases linearly with the total sliding area. Remarkably, the rate of increase is not dependent on the number (size) of the blocks. The energy absorbed was however ultimately higher for panels with fewer blocks (larger size) because the sliding area was higher. Finally, Fig. 6d shows the cumulated energy dissipated as a function of the total sliding area, but this time for different interlocking angles. Designs with  $\theta = 0^\circ$  show a constant increase of energy dissipated, but at lower slope compared to the other designs due to the lack of interlocking between the blocks (low strength,

rapid transition from stage I to II). At high angles ( $\theta = 10^\circ$ ) the rate of energy dissipation is initially the highest of all designs. However, the rate rapidly decreases and drops to zero. In these cases, the interlocking stresses are too high, which leads to excessive block damage and again precipitates deformation stage II. Therefore, the level of linearity on this type of data can be used as a measure of damage to individual blocks. The intermediate design ( $\theta = 5^\circ$ ) appears to be the best. The rate of energy absorption is relatively high, and is sustained throughout the experiment so the total energy dissipation becomes eventually higher than the  $\theta = 10^\circ$  case.

Compared to a monolithic plate, the architected panels are about four times less stiff, two times weaker in terms of maximum force, but their energy absorption is up to eight times higher. The area under the force-deflection curve for the architected panels represent energy dissipated by friction between the blocks. For monolithic ceramic however, much of the energy calculated from the area under the force-deflection curve is dissipated through dynamic effects, a well-documented phenomenon in fracture of brittle materials (Barinov, 1993). To measure the actual energy dissipated in the monolithic ceramic, we measured

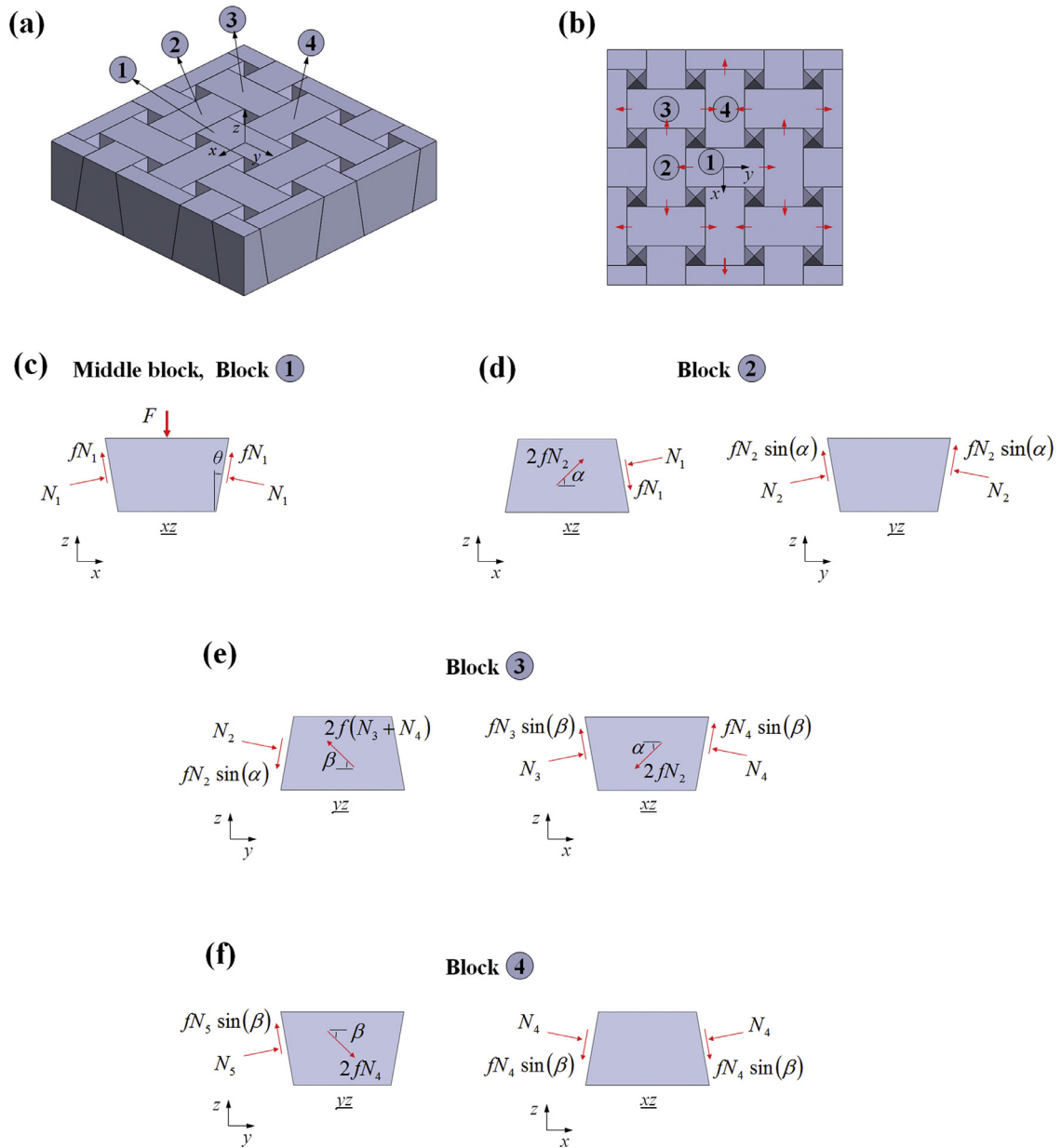


**Fig. 7.** The kinematics of the panel. (a) A  $3 \times 3$  samples showing the naming convention for the blocks. (b) An illustration showing how the load is transferred to the neighboring block. (c–f) The free body diagrams of the blocks 2–4. The forces are shown on the block cross-sections.  $N_2, N_3, N_4$  and  $N_5$  are the normal force between blocks [2 and 3], [3 and 4], [3 and peripheral block], and [4 and peripheral block] respectively.

the fracture toughness of alumina silicate following ASTM E 1820 (International, 2011) and found values of  $J_C = 35 \text{ J/m}^2$ . We then measured the total crack surface area in the monolithic ceramic, and multiplied it by the fracture toughness of the material to find  $\sim 10 \text{ mJ}$ , the actual energy dissipated in the material through formation of new surfaces. Considering this actual value of energy dissipation, the architected ceramics display a  $\sim 17$ -fold improvement in energy absorption in quasi-static loading.

**4. Simple analytical model based on kinematics**

The source of energy dissipation in architected panels is sliding and friction at the interfaces. We developed a simple analytical model to compute the amount of frictional energy dissipation in a  $3 \times 3$ -block panel. First, free body diagrams of the blocks were constructed (Fig. 7). 3D reconstruction showed the non-contacting

interfaces, for which the force was set to zero. For example, the middle block (block number 1) was in contact only with its neighbors along y direction, and therefore the forces in the interfaces along x direction were set to zero (Fig. 7c). The behavior of the interfaces was modeled using coulomb friction. The kinetic coefficient of friction  $f$  of alumina-silicate on alumina-silicate was experimentally measured following ASTM D1894 (ASTM, 1894), and was found to be  $f = 0.23$  (five samples were tested).

From the equilibrium of the middle block along the z direction, the normal force at the interfaces is  $N_1 = \frac{F}{2(\sin(\theta) + f \cos(\theta))}$  where  $F$  is the out-of-plane force exerted on the middle block,  $\theta$  is the interlocking angle,  $N_1$  is the normal force between blocks 1 and 2. The frictional force at this interface is therefore  $fN_1$ . Likewise, using the free-body diagram of the other blocks (Fig. 7d–f), the normal and frictional force applied through each of the interfaces were obtained as a function of applied load. The 3D reconstruction

data was then used to compute the sliding distances at the interfaces. By integration of the component of frictional force along the direction of sliding over the sliding distance for each of the interfaces, the total frictional energy dissipation was computed and was found to be 125 mJ for the  $3 \times 3$  sample with  $\theta = 2.5^\circ$ . This value of energy dissipation is  $\sim 30\%$  less than the area under the force deflection curve (172 mJ). We attributed this difference to the elastic energy stored in the panel. The panel tended to laterally expand under loading because of tapered shape of the blocks. As the lateral expansion was confined, in-plane compression was developed within the material. Part of this in-plane compression and in turn elastic energy was retained within the panel after the test was finished because the blocks jammed into each other.

## 5. Finite element modeling of the quasi-static behavior

3D reconstruction of the panels showed that the degradation of energy absorption with number of blocks is rooted in the decrease in total sliding area. To explore the effects of number (size) of block in more detail, we performed FEA of the panels. The geometries of  $3 \times 3$ ,  $5 \times 5$ , and  $7 \times 7$  panels with interlocking angle  $\theta = 2.5^\circ$  were constructed using Matlab (R 2016b, MA, US) and meshed/solved in ANSYS (2016 V16, PA, US), Fig. 8. The blocks were modeled as an isotropic linear elastic material. The elastic modulus of the material was obtained from three-point bending tests (four samples) and was found to be  $E = 18.7$  GPa (a result consistent with previous studies (Amrane et al., 2011)). The Poisson's ratio was assumed to be 0.2 which is typical of ceramics (Asmani et al., 2001). Coulomb friction model was used at the interfaces (friction coefficient  $f = 0.23$ ). The surfaces of the specimens for the friction coefficient measurement were prepared using the same cutting conditions which were used for the actual building blocks.

The geometry of a panel with  $\theta = 2.5^\circ$  and  $N \times N = 5 \times 5$  is shown on Fig. 8a. Because of the symmetries along the  $x$  and  $y$  axes, a quarter of the panel is modeled (Fig. 8b). Ten node quadratic elements were used to mesh the building blocks. The peripheral blocks were constrained in all directions. The symmetries were imposed along the  $yz$  and  $xz$  planes: the nodes on the  $yz$  plane ( $x = 0$ ) were constrained along the  $x$  direction ( $u_x = 0$ ) and the nodes on the  $xz$  plane ( $y = 0$ ) were constrained along the  $y$  direction ( $u_y = 0$ ). An out-of-plane displacement was applied on the node located at center of the panel ( $[x, y, z] = [0, 0, 0]$ ) and the reaction force  $F$  was captured as the middle block was pushed out of the panel. The mesh was refined until the force-deflection curve did not change with further mesh refinement. The converged results are plotted on Fig. 8c. The force is normalized by the elastic modulus of the material  $E$  and the length of the panel squared  $L^2$ . The displacement is normalized by the thickness of the panel  $h$ . The vertical displacement field  $u_z$  at six snapshots during loading (points A–F) and for panels with different number of blocks is shown on Fig. 8d. The results show similar trends as observed in the experiments, particularly, the panel resistance to deformation decreases with number of blocks (Fig. 8c).

We observed that the force  $F$  is almost proportional to the contact surface area between the middle block and its neighbors. To understand the reasons behind this proportionality, we looked at the distribution of the total contact stress at the interface between the middle block and its neighbor along  $y$  direction; i.e. the neighbor to which it interlocks (Fig. 8e). The force  $F$  is equilibrated by the contact forces at these interfaces. The mesh at these interfaces was refined until no change in the contour of contact stresses was observed. Fig. 8e shows that at the same displacement, the total contact stress at these interfaces are almost the same for different number of blocks. Since the contact surface area is larger for larger blocks, the resistance force also increases almost proportionally to the contact surfaces area. To explain why the contact stresses are

very similar for different number of blocks, we used the Winkler elastic foundation method which correlate the contact stress between two elastic bodies to their interference (Johnson and Johnson, 1987). We assumed that the blocks do not rotate, and only the middle block moves under loading. At a certain deflection, the interference  $\delta$  is the same for different number of blocks. This interference is accommodated by elastic deformation of half of the span  $L/2$  (Fig. 8f). The strains and in turn stresses are therefore the same for different number of blocks.

Although the contact surface area and therefore the material resistance to deformation are higher for larger blocks (lower  $N$ ), the flexural stress at the bottom of the indented block can be also higher in larger blocks because of their larger span. In this study, we did not observe flexural cracks in the architected panels and therefore the optimum performance was obtained with the largest blocks (i. e. lowest number of blocks  $N \times N = 3 \times 3$ ). However, the flexural stresses in the panels should also be considered as a limiting factor in the design of similar materials. FEA was useful in terms of exploring the effects of number of blocks. The predicted values of modulus and maximum force were however 1.5–3 times, and 14–15 times more than the experimental values respectively. The energy absorption predicted from the FEA models was also 9–13 times higher than the experimental and analytical results. We attributed these differences to presence of small gaps between the blocks resulted from statistical variations in the shape of blocks, an effect which has been previously found to significantly affect the mechanical performance in similar materials (Barthelat and Zhu, 2011). Moreover, our FEA model does not capture the brittle damages to the blocks which can significantly reduce the maximum force in the experiments. In the analytical model, the interface tractions were computed directly from the experimental force and therefore the computed tractions include the effects of gaps and brittle damages to the blocks. The energy absorption values predicted by the analytical model were therefore close to experiments and less than FEA predictions.

We also used FEA to study the behavior of TIM subjected to off-centered point forces.  $5 \times 5$  arrays of blocks with interlocking angle  $\theta = 2.5^\circ$  were subjected by to a point force applied at six different sites located at the center of six different blocks (Fig. 9a). These six cases cover all possible sites for a  $5 \times 5$  array because of symmetries. All other boundary conditions, element type/size, and materials properties were kept the same as the previous simulations. In all six cases, we observed that sliding mainly occurred at the indented block, the rest of the panel remaining largely intact. As a result, the force-deflection curves were very similar for all cases (Fig. 9b). Point forces applied away from the center of the panel resulted in slight increase of stiffness and maximum force and a slight decrease in maximum deflection. In this study, we focused on the panels with odd number of blocks to compare different panels loaded in the center of the center block in the panel. However, very large blocks would break under flexural stress, in a way which converges towards the response of the monolithic panel.

## 6. Impact response

We finally assessed the resistance to impact of our architected panels (Fig. 10). We focused on blocks with interlocking angle  $\theta = 5^\circ$  which gave the optimum results in quasi-static conditions.  $3 \times 3$ ,  $5 \times 5$ , and  $7 \times 7$  panels were tested (one sample per panel). We held the panels in the same frame as the one used for the quasi-static tests, and a 1030 g impactor (Instron CEAST, MA, US) with the same tip geometry as the quasi-static test was dropped at a speed of 0.75 m/s, which is representative of an intermediate impact speed (Fig. 10a). The impact was instrumented, and the force history was recorded by a 3 kN piezoelectric load cell embedded in the impactor. We also captured high-speed stereo-images of

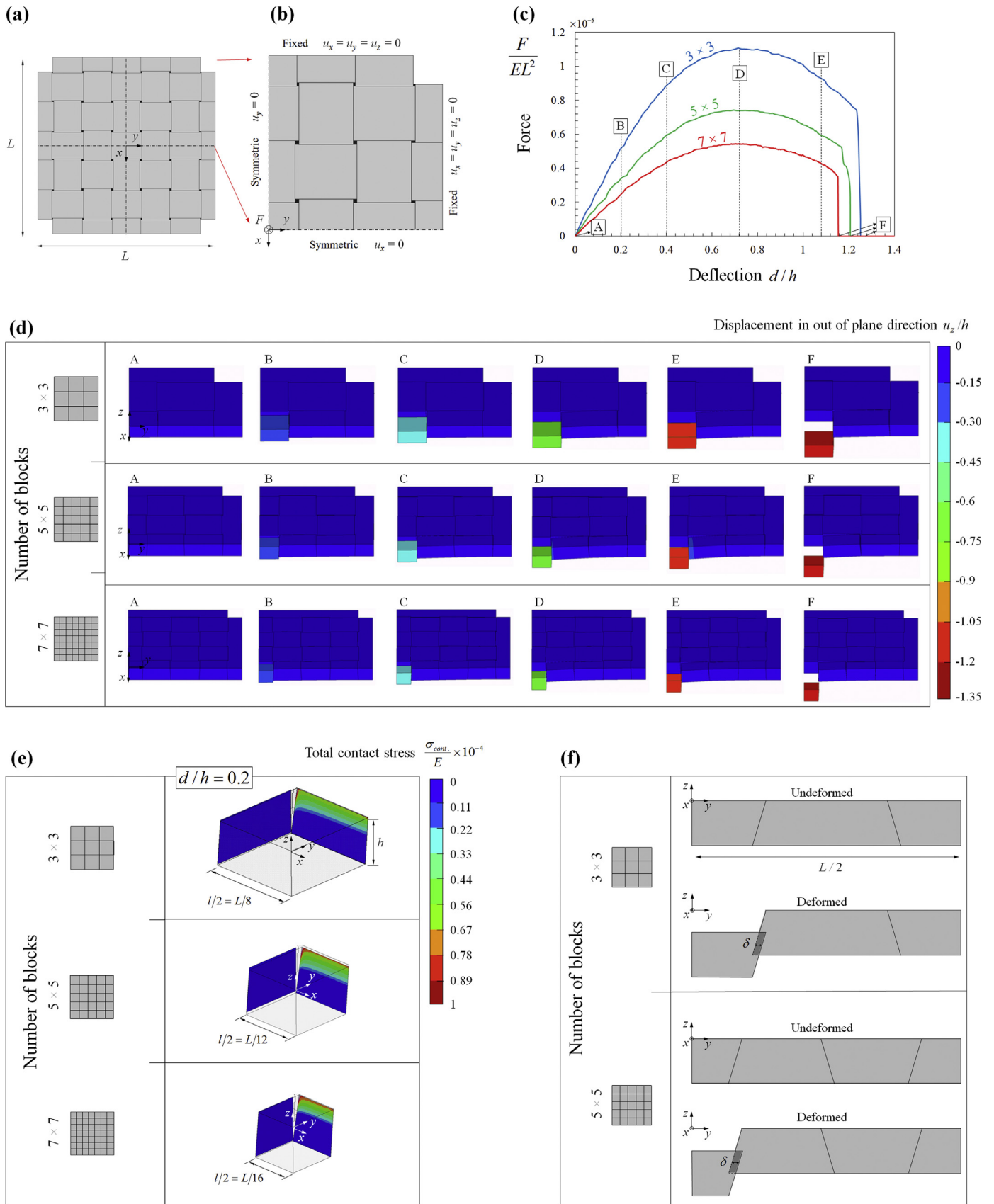


**Fig. 8.** Finite element model of the panel. (a) A 5 × 5 assembly of the blocks with interlocking angle  $\theta = 2.5^\circ$  (b) A quarter of the assembly is modeled because of the symmetries along the  $x$  and  $y$  axes. The boundary conditions are also shown. (c) Normalized force-normalized deflection behavior of the panels with the same interlocking angle  $\theta = 2.5^\circ$  but different number of blocks. (d) The out-of-plane displacement of the blocks at various stages of loading and for panels with different number of blocks. (e) The total contact stress at the interface. (f) Deformation diagram showing the interference between the blocks.

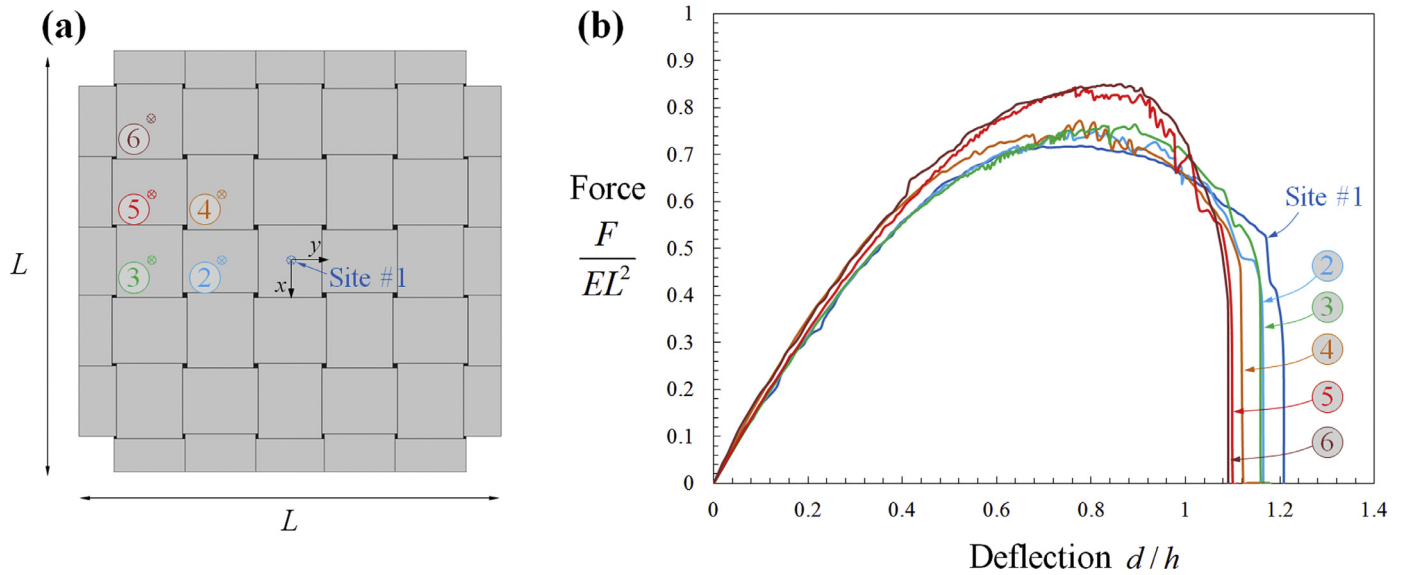


**Fig. 9.** Effects of puncture location on the behavior of the panel. (a)  $5 \times 5$  assembly of the blocks with interlocking angle  $\theta = 2.5^\circ$  showing the six sites for the point force; (b) normalized force-normalized deflection curves of the panels loaded at the 6 representative puncture sites.

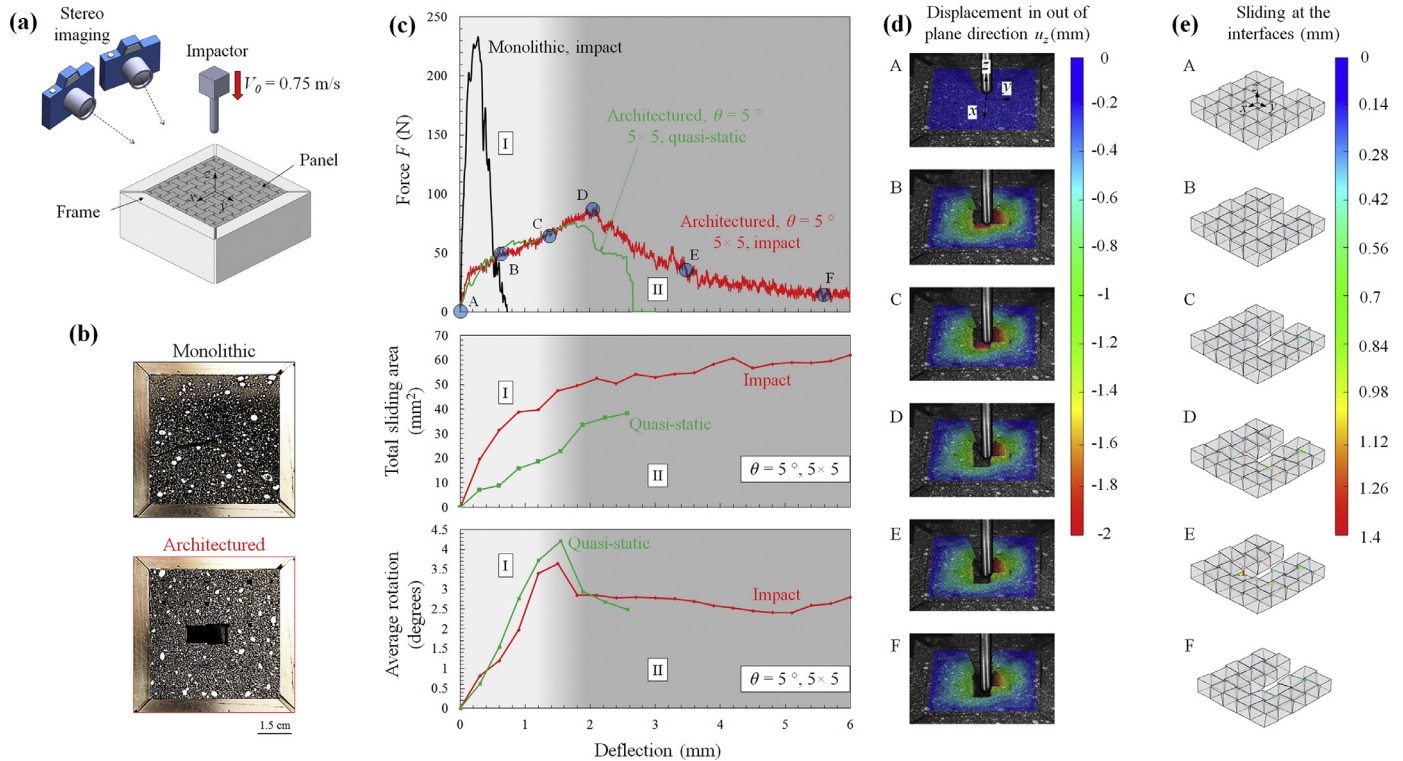


**Fig. 10.** Impact testing of architected panels. (a) The schematic of the impact test apparatus. (b) The post-mortem samples: architected and monolithic. (c) The force-displacement behavior of the architected ceramics compared to monolithic ceramic. (d) The displacement field in  $z$  direction at six stages loading. (e) the 3D reconstructed panels showing the values of sliding at the interfaces.

the samples with the same setup as the quasi-static test, at a rate of about 1000 frames/second. Monolithic ceramic panels were also impacted for reference. Fig. 10c shows the force-deflection curve of a  $5 \times 5$ -block panel with  $\theta = 5^\circ$ . Like quasi-static tests, the monolithic and architected ceramic panels showed major differences in terms of performance and failure modes (Fig. 10b–d). Under impact loading, the monolithic ceramic panel elastically deformed until several flexural cracks initiated at the impact site and propagated to the edges. The panel broke at a deflection of  $\sim 0.2$  mm and at a force of  $\sim 235$  N which is  $\sim 14\%$  higher than the values obtained

in the quasi-static tests. The difference in the maximum force is small and may be explained by the sub-critical crack growth in quasi-static loading, a well-studied phenomenon in the brittle materials (Johnson and Paris, 1968; Ravichandran and Subhash, 1995). The drop of force for the monolithic plate was also more progressive in dynamic condition, because the inertia of the broken pieces generated a resisting force (Harrigan et al., 1999). The architected panels deformed and failed in a way which was similar to the quasi-static tests: the force-displacement curve had the same bell-shape characteristics (Fig. 10c), and 3D reconstruction

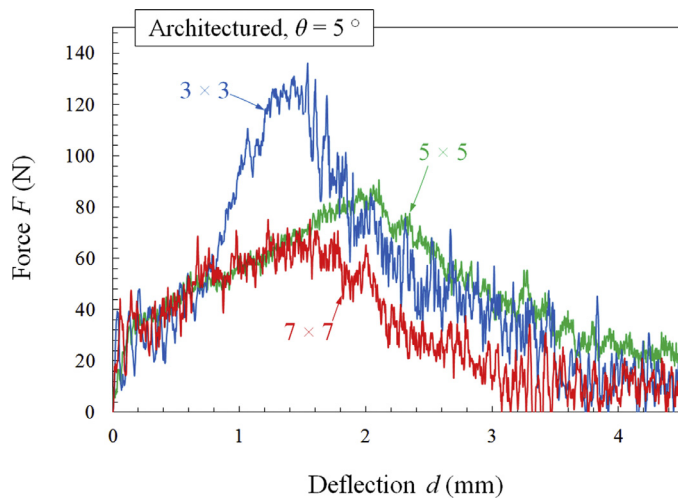


**Fig. 11.** The effect of number of blocks on the impact behavior. The force-displacement curves of panels with  $\theta = 5^\circ$  and with different number of blocks ( $3 \times 3$ ,  $5 \times 5$ , and  $7 \times 7$ ).

revealed similar deformation/failure mechanisms (Fig. 10d and e). While the panels' stiffness was almost unaffected by the loading rate, their strength and particularly energy absorption increased in impact loading. For example, with the  $5 \times 5$ -block panel (Fig. 10), the strength and energy absorption are 22% and 51% higher in impact compared to quasi-static conditions. The increase of strength was again attributed to the sub-critical crack growth in quasi-static loading; i. e. the surface damage of the blocks was delayed in impact.

The analysis of the stereo images provided insights into the micro-mechanics of deformation of the blocks and panels, which in turn were used to explain the rate effects. To study inertia effects, we obtained the average velocity of each block in out-of-plane direction at the time of impact using the 3D reconstructed data. We first observed that the center block quickly reached the velocity of impactor ( $V_0 = 0.75$  m/s) upon impact. At each time in the experiment, we also found that the velocity of the blocks decreased almost linearly from the center block to the peripheral blocks which remained stationary. Having the mass of each block ( $\sim 0.6$  g for a  $5 \times 5$ -block panel), the total kinetic energy of the panel was found to be  $\sim 6$  mJ. The inertia effects alone therefore could not explain the difference between the energy absorption of the panels in quasi-static and impact tests (the difference is  $\sim 85$  mJ for a  $5 \times 5$ -block panel with  $\theta = 5^\circ$ ). We also noticed differences in the way panels deformed and failed between impact and quasi-static loading. To quantify these differences, we measured the total sliding area and the average rotation of the individual blocks during loading (Fig. 10c). We found that the total sliding area was significantly larger in impact loading, while average rotation of individual blocks was slightly lower. We attributed these effects to a decreased dynamic coefficient of friction at higher rate (a well-documented rate effect in ceramics Di Toro et al., 2011; Johannes et al., 1973). The reduced coefficient of friction results in lower frictional stresses which prevented or delayed surface damage on the blocks, promoting effective energy dissipation. Attenuation of the elastic waves by the periodic structure of the material might also contribute to the improved energy absorption of the panels in impact loading (Davies et al., 2014).

Finally, we found that the mechanical performance degraded with the number of blocks (Fig. 11), just like in the quasi-static tests. Increasing the number of blocks from  $3 \times 3$  to  $5 \times 5$  resulted in 3%, 33%, and 18% decrease in stiffness, strength, and energy absorption. Increasing it further to  $7 \times 7$  resulted in 5%, 17% and

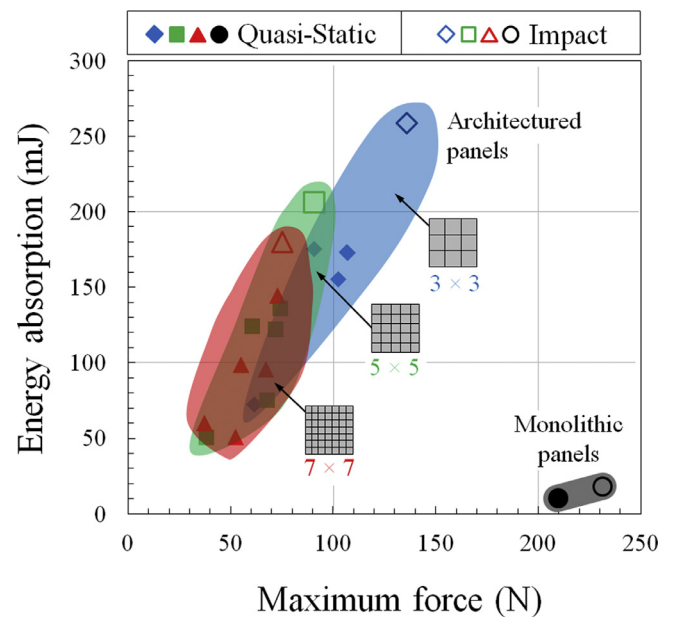


**Fig. 12.** Material performance chart that summarizes the maximum force and the energy absorption for monolithic and architected panels, in quasi-static and impact conditions.

14% further decrease in these properties respectively. These trends were again attributed to the lower total sliding area and lower contact surface area between the middle block and its neighbors when blocks are smaller. The impact resistance of the panels with different number of blocks and  $\theta = 5^\circ$  was 2.5 to 3.5 times higher than the monolithic ceramic in energy terms. However, considering the actual energy absorbed in the monolithic panels by formation of cracks ( $\sim 13$  mJ), the impact resistance of architected panels was 13–20 times higher than monolithic ones.

## 7. Summary and outlook

Structural materials with attractive combinations of strength and toughness together with other functionalities such as multi-hit capability, damage sensing and self-repair have been a long-standing objective in materials research. Introducing a “mesoscale” architecture in materials is a promising strategy to achieve these performances and features, a strategy which has been successfully used in nature for millions of years in materials like nacre or bone. In this work, we demonstrate how segmenting a monolithic ceramic plate into interlocking blocks can completely change its mechanisms of deformation and fracture, and can lead to pseudo ductility, energy absorption, impact resistance and damage tolerance in an otherwise all brittle ceramic. Moreover, our fabrication strategy is simple, versatile and scalable.

A summary of the mechanical performance of the architected panels is shown on a material performance chart (Fig. 12): The strength of the architected panel is 1/4 to 1/2 of the strength of the monolithic panel. This is a common characteristics of architected systems, because introducing frictional interfaces in the systems tends to decrease stiffness and strength (A lower stiffness may actually be an advantage for flexible protection Martini et al., 2017). More significantly, we found that the energy absorption of the architected panels is 5 to 20 times greater than the monolithic material. This remarkable improvement makes the panel damage resistant, which can be critical for applications where kinetic energy from impacts must be absorbed, and where energy absorption is more important than strength and stiffness. Here we demonstrate that architected panels can achieve very high

impact resistance, without sacrificing the surface hardness and durability of the ceramic material. For the first time, we report the three-dimensional reconstruction of architected panels from stereo-imaging which leads to unique insights into the deformation mechanisms in these materials. An initial stage (I) consists of simultaneous sliding and rotation of the blocks. In this stage the loss of contact area is offset by geometric hardening and progressive interlocking. The system then transitions into a stage (II) where most of the deflection is absorbed by the pushing out of the center block. In terms of optimizing performance, the transition from mode I to II must be delayed as much as possible. This transition is triggered by a geometric instability when the interlocking angle is too low (case  $\theta = 0^\circ$ ) or by damage of the blocks and associated loss of load bearing capability when the interlocking is too high (case  $\theta = 10^\circ$ ). Here we found that  $\theta = 5^\circ$  was the optimum interlocking angle.

That transition can also be delayed by lowering the coefficient of friction (which was achieved in the impact regime), which translated into a delayed I→II transition, more uniformly distributed nonlinear deformation, extended stage II and much larger energy absorption. FEA simulations can be helpful in future to study these rate effects in more depth. Interestingly, we recently came to a similar conclusion for jigsaw-like interlocked structure, where we found that lower coefficients of friction delay undesirable fracture from frictional contact stresses, which in turn leads to better designs in terms of energy absorption (Malik et al., 2017). Finally, we found that increasing the number of blocks (i.e. using smaller blocks) degrade all the properties (Fig. 12) partially due to decrease in the sliding area. Also, finite element analyses revealed that the contact pressure at the interface only depends on the interlocking angle and is not dependant on the size of the blocks. Larger blocks, with greater contact area with neighboring blocks, offer more resistance to sliding and more energy absorption. All the panels we tested in this study failed by push-out of the central block, while the rest of the material was left slightly deformed but largely intact. This segmentation strategy can therefore lead to systems which are damage tolerant with “multi-hit” capabilities. Individual blocks never failed by flexural fracture, but it is conceivable that this failure mode can occur if the blocks are too large, just like flexural failure prevails in monolithic panels. Flexural failure must be avoided because it shuts off all energy dissipative mechanisms, and this particular failure mode is therefore likely to be a limiting factor for the size of the blocks. The panels proposed here can find applications in armored protection or for thermal barrier systems (Amrane et al., 2011). This work finally demonstrates how the concept of material architecture can be used to precisely program the mechanics and performance of materials. More generally this type of system behave in ways that contradict standard paradigms in materials: larger size features (larger blocks) lead to stronger materials, but larger blocks also mean that the separation of length scales between microstructure and component size, a requirement for property homogenization, is not possible (Ostoja-Starzewski, 2006). Finally, there is an infinite number of possible architectures to make materials and structures (Dyskin et al., 2001). Varying the shapes and arrangement of the building blocks in two and three dimensions, exploring different loading configurations (distributed loads, forces with a tangential component...), and considering different interface properties (e. g. a soft polymeric interface) to create new mechanisms and properties represents a rich landscape which is yet to explore.

## Acknowledgments

This work was funded by a NSERC Strategic Grant and by the Security, Materials, and Technologies (SMT) program at National Research Council of Canada. M. Mirkhalaf was partially supported

by a FQRNT (Fonds Quebecois de la Recherche sur la Nature et les Technologies) postdoctoral award. We also acknowledge Daniel O’Keefe and Hugo Laurin for their help in preparing the cutting set-up.

## References

- Aizenberg, J., Weaver, J.C., Thanawala, M.S., Sundar, V.C., Morse, D.E., Fratzl, P., 2005. Skeleton of *Euplectella* sp.: structural hierarchy from the nanoscale to the macroscale. *Science* 309, 275–278.
- Amrane, B., Ouedraogo, E., Mamen, B., Djaknoun, S., Mesrati, N., 2011. Experimental study of the thermo-mechanical behaviour of alumina-silicate refractory materials based on a mixture of Algerian kaolinic clays. *Ceram. Int.* 37, 3217–3227.
- Asmani, M., Kermel, C., Leriche, A., Ourak, M., 2001. Influence of porosity on Young’s modulus and Poisson’s ratio in alumina ceramics. *J. Eur. Ceram. Soc.* 21, 1081–1086.
- ASTM, 1894. Standard Test Method for Static and Kinetic Coefficients of Friction of Plastic Film and Sheeting. American Society for Testing and Materials.
- Autruffe, A., Pelloux, F., Brugger, C., Duval, P., Brechet, Y., Fivel, M., 2007. Indentation behaviour of interlocked structures made of ice: Influence of the friction coefficient. *Adv. Eng. Mater.* 9, 664–666.
- Barinov, S., 1993. Work-of-fracture determination for brittle materials. *J. Mater. Sci. Lett.* 12, 674–676.
- Barthelat, F., 2015. Architected materials in engineering and biology: fabrication, structure, mechanics and performance. *Int. Mater. Rev.* 60, 413–430.
- Barthelat, F., Rabiei, R., 2011. Toughness amplification in natural composites. *J. Mech. Phys. Solids* 59, 829–840.
- Barthelat, F., Yin, Z., Buehler, M.J., 2016. Structure and mechanics of interfaces in biological materials. *Nat. Rev. Mater.* 1, 16007.
- Barthelat, F., Zhu, D., 2011. A novel biomimetic material duplicating the structure and mechanics of natural nacre. *J. Mater. Res.* 26, 1203–1215.
- Brechet, Y., Embury, J., 2013. Architected materials: expanding materials space. *Scr. Mater.* 68, 1–3.
- Brocato, M., Mondardini, L., 2012. A new type of stone dome based on Abeille’s bond. *Int. J. Solids Struct.* 49, 1786–1801.
- Chintapalli, R.K., Mirkhalaf, M., Dastjerdi, A.K., Barthelat, F., 2014. Fabrication, testing and modeling of a new flexible armor inspired from natural fish scales and osteoderms. *Bioinspiration Biomimetics* 9, 036005.
- Davies, B., King, A., Newman, P., Minett, A., Dunstan, C.R., Zreiqat, H., 2014. Hypothesis: bones toughness arises from the suppression of elastic waves. *Sci. Rep.* 4.
- Di Toro, G., Han, R., Hirose, T., De Paola, N., Nielsen, S., Mizoguchi, K., Ferri, F., Cocco, M., Shimamoto, T., 2011. Fault lubrication during earthquakes. *Nature* 471, 494–498.
- Djumas, L., Simon, G.P., Estrin, Y., Molotnikov, A., 2017. Deformation mechanics of non-planar topologically interlocked assemblies with structural hierarchy and varying geometry. *Sci. Rep.* 7, 11844.
- Dugue, M., Fivel, M., Brechet, Y., Dendievel, R., 2013. Indentation of interlocked assemblies: 3D discrete simulations and experiments. *Comput. Mater. Sci.* 79, 591–598.
- Dyskin, A., Estrin, Y., Kanel-Belov, A., Pasternak, E., 2003a. Topological interlocking of platonic solids: a way to new materials and structures. *Philos. Mag. Lett.* 83, 197–203.
- Dyskin, A.V., Estrin, Y., Kanel-Belov, A.J., Pasternak, E., 2001. Toughening by fragmentation - how topology helps. *Adv. Eng. Mater.* 3, 885–888.
- Dyskin, A.V., Estrin, Y., Pasternak, E., Khor, H.C., Kanel-Belov, A.J., 2003b. Fracture resistant structures based on topological interlocking with non-planar contacts. *Adv. Eng. Mater.* 5, 116–119.
- Estrin, Y., Dyskin, A., Pasternak, E., Schaare, S., Stanchits, S., Kanel-Belov, A., 2004. Negative stiffness of a layer with topologically interlocked elements. *Scr. Mater.* 50, 291–294.
- Evans, A.G., 1990. Perspective on the development of high-toughness ceramics. *J. Am. Ceram. Soc.* 73, 187–206.
- Feng, Y., Siegmund, T., Habtour, E., Riddick, J., 2015. Impact mechanics of topologically interlocked material assemblies. *Int. J. Impact Eng.* 75, 140–149.
- Habelitz, S., Marshall, S., Marshall, G., Balooch, M., 2001. Mechanical properties of human dental enamel on the nanometre scale. *Arch. Oral. Biol.* 46, 173–183.
- Haldar, S., Sain, T., Ghosh, S., 2017. A novel high symmetry interlocking micro-architecture design for polymer composites with improved mechanical properties. *Int. J. Solids Struct.* 124, 161–175.
- Harrigan, J., Reid, S., Peng, C., 1999. Inertia effects in impact energy absorbing materials and structures. *Int. J. Impact Eng.* 22, 955–979.
- International, A., 2011. Standard Test Method for Measurement of Fracture Toughness. ASTM International.
- Jackson, A.P., Vincent, J.F.V., Turner, R.M., 1988. The mechanical design of nacre. *Proc. R. Soc. Lond.* 234, 415–440.
- Javan, A.R., Seifi, H., Xu, S., Ruan, D., Xie, Y., 2017. The impact behaviour of plate-like assemblies made of new interlocking bricks: An experimental study. *Mater. Des.*
- Johannes, V., Green, M., Brockley, C., 1973. The role of the rate of application of the tangential force in determining the static friction coefficient. *Wear* 24, 381–385.
- Johnson, H.H., Paris, P.C., 1968. Sub-critical flaw growth. *Eng. Fract. Mech.* 1, 3–45.
- Johnson, K.L., Johnson, K.L., 1987. *Contact Mechanics*. Cambridge university press.
- Khandelwal, S., Siegmund, T., Cipra, R., Bolton, J., 2012. Transverse loading of cellular topologically interlocked materials. *Int. J. Solids Struct.* 49, 2394–2403.

- Khandelwal, S., Siegmund, T., Cipra, R., Bolton, J., 2015. Adaptive mechanical properties of topologically interlocking material systems. *Smart Mater. Struct.* 24, 045037.
- Khandelwal, S., Siegmund, T., Cipra, R.J., Bolton, J.S., 2014. Scaling of the elastic behavior of two-dimensional topologically interlocked materials under transverse loading. *J. Appl. Mech. Trans. ASME* 81, 031011–031019.
- Koester, K.J., Ager, J., Ritchie, R., 2008. The true toughness of human cortical bone measured with realistically short cracks. *Nat. Mater.* 7, 672–677.
- Krause, T., Molotnikov, A., Carlesso, M., Rente, J., Rezwani, K., Estrin, Y., Koch, D., 2012. Mechanical properties of topologically interlocked structures with elements produced by freeze gelation of ceramic slurries. *Adv. Eng. Mater.* 14, 335–341.
- Lin, E., Li, Y., Ortiz, C., Boyce, M.C., 2014. 3D printed, bio-inspired prototypes and analytical models for structured suture interfaces with geometrically-tuned deformation and failure behavior. *J. Mech. Phys. Solids* 73, 166–182.
- Malik, I., Mirkhalaf, M., Barthelat, F., 2017. Bio-inspired “jigsaw”-like interlocking sutures: Modeling, optimization, 3D printing and testing. *J. Mech. Phys. Solids* 102, 224–238.
- Martini, R., Balit, Y., Barthelat, F., 2017. A comparative study of bio-inspired protective scales using 3D printing and mechanical testing. *Acta Biomater.* 55, 360–372.
- Mather, A., 2007. Concepts in Improved Product Manufacturability and Reusability Through the Use of Topologically Interconnecting Structural Elements. Purdue University, West Lafayette, IN.
- Mather, A., Cipra, R., Siegmund, T., 2012. Structural integrity during remanufacture of a topologically interlocked material. *Int. J. Struct. Integr.* 3, 61–78.
- Mirkhalaf, M., Ashrafi, B., 2017. A numerical study on improving the specific properties of staggered composites by incorporating voids. *Mater. Today Commun.*
- Mirkhalaf, M., Barrett, C.J., Barthelat, F., 2015. Self-assembly of microscopic tablets within polymeric thin films: a possible pathway towards new hybrid materials. *RSC Adv.* 5, 4780–4787.
- Mirkhalaf, M., Barthelat, F., 2015. A laser-engraved glass duplicating the structure, mechanics and performance of natural nacre. *Bioinspiration Biomimetics* 10, 026005.
- Mirkhalaf, M., Barthelat, F., 2016. Nacre-like materials using a simple doctor blading technique: fabrication, testing and modeling. *J. Mech. Behav. Biomed. Mater.* 56, 23–33.
- Mirkhalaf, M., Barthelat, F., 2017. Design, 3D printing and testing of architected materials with bistable interlocks. *Extreme Mech. Lett.* 11, 1–7.
- Mirkhalaf, M., Dastjerdi, A.K., Barthelat, F., 2014. Overcoming the brittleness of glass through bio-inspiration and micro-architecture. *Nat. Commun.* 5, 3166.
- Mirkhalaf, M., Tanguay, J., Barthelat, F., 2016. Carving 3D architectures within glass: exploring new strategies to transform the mechanics and performance of materials. *Extreme Mech. Lett.* 7, 104–113.
- Mirkhalaf, M., Zhou, T., Barthelat, F., 2018. Simultaneous improvements of strength and toughness in topologically interlocked ceramics. *Proc. Natl. Acad. Sci.* published ahead of print August 23, 2018, <https://doi.org/10.1073/pnas.1807272115>.
- Ostoja-Starzewski, M., 2006. Material spatial randomness: from statistical to representative volume element. *Probab. Eng. Mech.* 21, 112–132.
- Ravichandran, G., Subhash, G., 1995. A micromechanical model for high strain rate behavior of ceramics. *Int. J. Solids Struct.* 32, 2627–2646.
- Ritchie, R.O., 2011. The conflicts between strength and toughness. *Nat. Mater.* 10, 817–822.
- Rudykh, S., Ortiz, C., Boyce, M.C., 2015. Flexibility and protection by design: imbricated hybrid microstructures of bio-inspired armor. *Soft Matter* 11, 2547–2554.
- Schaare, S., Dyskin, A., Estrin, Y., Arndt, S., Pasternak, E., Kanel-Belov, A., 2008. Point loading of assemblies of interlocked cube-shaped elements. *Int. J. Eng. Sci.* 46, 1228–1238.
- Siegmund, T., Barthelat, F., Cipra, R., Habtour, E., Riddick, J., 2016. Manufacture and mechanics of topologically interlocked material assemblies. *Appl. Mech. Rev.* 68, 040803.
- Siegmund, T., Khandelwal, S., Wheatley, B., Varanasi, S., Cipra, R., Bolton, S., 2013. Multifunctional composites by segmentation and assembly. In: International Conference on Composite Materials (ICCM-19), Montreal, QC, Canada, July, pp. 23–31.
- Slesarenko, V., Kazarinov, N., Rudykh, S., 2017a. Distinct failure modes in bio-inspired 3D-printed staggered composites under non-aligned loadings. *Smart Mater. Struct.* 26, 035053.
- Slesarenko, V., Volokh, K.Y., Aboudi, J., Rudykh, S., 2017b. Understanding the strength of bioinspired soft composites. *Int. J. Mech. Sci.* 131, 171–178.
- Wang, R.Z., Suo, Z., Evans, A.G., Yao, N., Aksay, I.A., 2001. Deformation mechanisms in nacre. *J. Mater. Res.* 16, 2485–2493.
- Yahyazadehfard, M., Ivancik, J., Majid, H., An, B., Zhang, D., Arola, D., 2014. On the mechanics of fatigue and fracture in teeth. *Appl. Mech. Rev.* 66, 030803.